Flight Forces and Altitude Regulation of 12 gram I-Bird

Stanley S. Baek and Ronald S. Fearing

***Abstract*— Ornithopter flight forces are typically measured with the body fixed to a force sensor. Here, we demonstrate the identification of free flight aerodynamic forces at a stable equilibrium point of an ornithopter and compare them with the tethered flight aerodynamic forces. For this demonstration, we have developed a closed-loop altitude regulation for the ornithopter using an external camera and custom made onboard electronics. The results show that the tethered aerodynamic force measurement of a 12 gram ornithopter with zero induced velocity underestimates the total flight force by 24.8 mN.**

I. INTRODUCTION

Flapping-wing flight in nature has unparalleled maneuverability, agility, and hovering capability. Over the last few decades, engineers have made remarkable progress toward the design of flapping-wing micro air-vehicles (MAVs) inspired by biological systems [1], [7], [8], [10], [13], [14]. However, accurate measurement of free flight aerodynamic forces in their design process is a recurring issue. This is because enough lift force must be generated while simultaneously achieving a stable equilibria for user defined flight. Indeed, control engineers are usually interested in the free flight aerodynamic forces of air-vehicles near the stable equilibria. Then, we can measure accelerations of the body in air to estimate the controlled free flight aerodynamic forces for given input signals, such as wing velocity, rudder position, etc.

The aerodynamic forces have been measured with a force/torque sensor, such as a load cell [9] or double cantilevers with strain gauges [15]. Wind tunnel measurements have also been conducted to measure lift and thrust forces simultaneously [5]. Although tethered measurement provides a good approximation of aerodynamic forces before free flight, the difference between the measured forces and the real forces aloft could be unacceptably large. There are several reasons for the difference between free flight and tethered measurements. First, the fixed body of the ornithopter and structural compliance can give rise to vibrations which either absorb propulsive power or change wing stroke kinematics. Second, estimating flight force directions in free flight is inherently noisy.

Some of the significant research on the development of closed-loop control of flapping-wing MAVs is summarized here. Deng *et al*. [2] have designed LQR-based feedback laws for hovering control using an approximated time-invariant model of Micromechanical Flying Insect [3] with time average aerodynamic forces. Khan *el al*. have also developed a differential flatness based nonlinear controller for a time-averaged system that can be applied to flapping-wing MAVs such as FWMAV [6]. These works have performed well in computer simulations, yet they have not been implemented in a real flapping wing robot. Other development of closed-loop control for a flapping wing MAVs have been demonstrated by Shigeoka [11]. Acquiring acceleration and position data using an accelerometer and a VICON motion tracking system, Shigeoka has developed a simple dynamic model for an MAV and demonstrated simulation results using frequency analysis.

Fig. 1. The modified 12 gram flapping wing robot with custom made electronics.

In this paper, we demonstrate closed-loop altitude regulation for an ornithopter using an external camera and an onboard microprocessor. With this stable height control, we present a method of identification of aerodynamic forces near the stable equilibrium. Then, we compare these forces with the tethered flight forces measured with a load cell.

II. ORNITHOPTER PLATFORM

The flapping-wing robot used in this work has been modified from a toy ornithopter, Silverlit WingMaster I-Bird as shown in Fig. 1. From the original 4 winged ornithopter, the styrofoam outer body has been removed to reduce the weight. The removal of styrofoam, however, results in undesirable bending and torsional compliance of the structure that absorbs some of the power to be transferred to the

S. Baek is with the Department of Electrical Engineering and Computer Sciences, University of California, Berkeley, CA 94720, USA stanbaek@eecs.berkeley.edu

R. Fearing is with the Department of Electrical Engineering and Computer Sciences, University of California, Berkeley, CA 94720, USA ronf@eecs.berkeley.edu

TABLE I

SPECIFICATIONS OF THE MODIFIED ORNITHOPTER

Wing Span	28 cm
Battery	60 mAh Li-Poly with 1.6 grams
DC motor	1.6 grams
Motor board	0.25 grams
Bluetooth module	0.9 grams
MCU board	0.75 grams
Total Weight	12.4 grams

environment. As a result, the aerodynamic forces generated by the wings are significantly reduced. To compensate for this, we have replaced the main backbone frame with a stiff carbon fiber tube so that the aerodynamic forces remain the same. The original RC electronics have also been replaced with custom made electronics. The new electronics consist of a motor board, an IR camera, a microprocessor board, and a Bluetooth module. The motor board has one MOSFET and two H-Bridges making it capable of of driving up to three DC motors at the same time (Fig. 2). It also has two differential amplifiers with low pass filters to measure the back-EMF voltages of two motors[1]. The IR camera is to detect IR emitters, but it is not used in this work. The microprocessor consists of a 16-bit microcontroller running at 40MHz and a 2MB DataFlash memory. The Bluetooth 2.0 module is used for wireless communication with a PC (for more details about the microprocessor board and the Bluetooth module, please refer to [4]).

A 60 mAh Lithium-Polymer battery provides power for the electronics, the DC motor to drive the flapping wings, and a magnetic actuator to steer the rudder at the tail of the ornithopter. The DC motor can drive the wings at 17-20 Hz depending on battery charge. The battery has been carefully mounted on the body of the ornithopter so that we can achieve pendulum-like passive stability. The specifications of the modified ornithopter are summarized in Table I.

III. AERODYNAMIC MODEL

Figure 3 depicts the coordinate systems and relevant forces acting on the body of the ornithopter. The origin of the body coordinates ($\mathbf{e_t}$, $\mathbf{e_n}$) is attached to the center of mass of the ornithopter. The tangential axis of the body coordinate, $\mathbf{e_t}$, is defined as the line from the center of mass, $\mathbf{c}$, passing through the point, $\mathbf{r}$, on which the resultant aerodynamic forces are acting, and the normal axis of the coordinate, $\mathbf{e_n}$, is perpendicular to the tangential axis. The equations of motion in the body coordinate are given by

$$m\ddot{x}_b - m\dot{\phi}\dot{y}_b = -mg\sin\phi + F_T \quad (1)$$

$$m\ddot{y}_b + m\dot{\phi}\dot{x}_b = -mg\cos\phi + F_N \quad (2)$$

$$I\ddot{\phi} = dF_N \quad (3)$$

where F_T is the tangential force in the $\mathbf{e_t}$ direction, F_N is the normal force in the $\mathbf{e_n}$ direction, x_b is the displacement

[1]Any two motors can be chosen for back-EMF measurement by populating the resistors between the input port of amplifiers and the desired motor nodes.

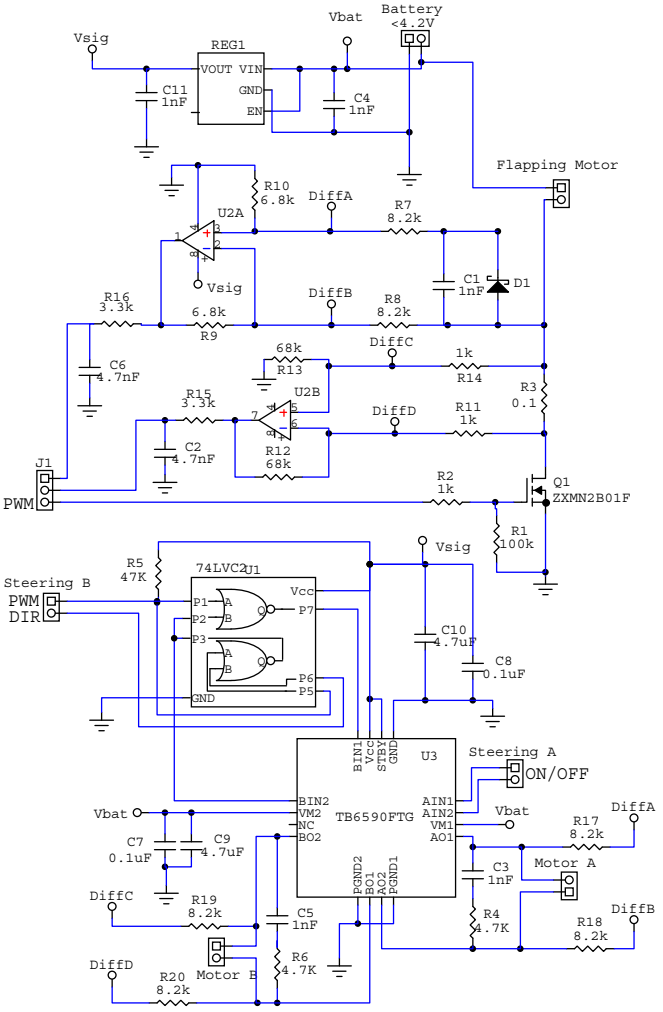

Fig. 2. Schematics of the 0.25 gram motor driver board. It can drive up to 3 motors at the same time.

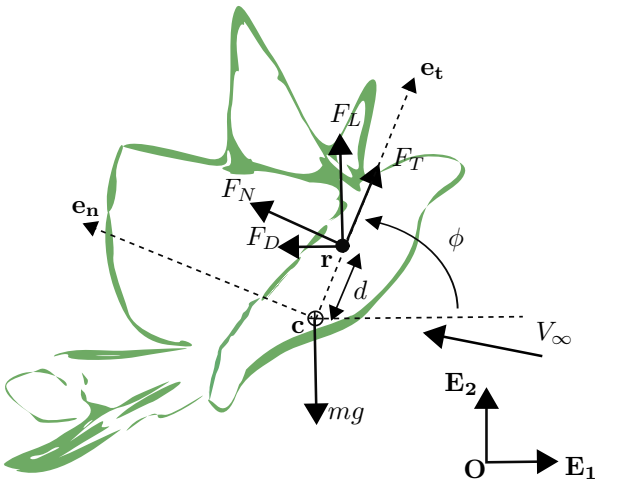

Fig. 3. The coordinate systems and the forces acting on the body of ornithopter.

in the $\mathbf{e_t}$ direction, y_b is the displacement in the $\mathbf{e_n}$ direction, ϕ is the angle between $\mathbf{e_1}$ and $\mathbf{E_1}$, d is the distance between the center of mass and the origin of the forces, m is the mass of the ornithopter, I is the moment of inertia, and g is the gravitational acceleration. The equations of motion can also be written in the inertial frame ($\mathbf{E_1}$, $\mathbf{E_2}$) fixed to the ground as follows

$$m\ddot{x} = -F_D \quad (4)$$
$$m\ddot{y} = -mg + F_L \quad (5)$$
$$I\ddot{\phi} = dF_L \cos\phi + dF_D \sin\phi \quad (6)$$

where x is the displacement in the $\mathbf{E_1}$ direction, y is the displacement in the $\mathbf{E_2}$ direction, F_L is the lift force in the $\mathbf{E_2}$ direction, and F_D is the drag force in the $-\mathbf{E_1}$ direction. The relationship between (F_L, F_D) and (F_T, F_N) is given by

$$F_L = F_T \sin\phi + F_N \cos\phi \quad (7)$$
$$F_D = -F_T \cos\phi + F_N \sin\phi \quad (8)$$

It is important to note that the aerodynamic forces, $\mathbf{F}$ = (F_T, F_N, F_L, F_D), are functions of the wing velocity ω, the induced velocity V_∞, and the angle of attack α (the angle between the tangential axis and the direction of the induced velocity). Furthermore, $\mathbf{F}$ can be decomposed into the following two functions

$$\mathbf{F} = \mathbf{F}(V_\infty, \omega, \alpha) = \mathbf{F}^w(\omega) + \mathbf{F}^i(V_\infty, \alpha)$$

where $\mathbf{F}^w(\omega)$ is the force solely generated by the flapping motion of the wings while the body of the ornithopter is stationary, i.e., $\dot{x}_b$ = 0 and $\dot{y}_b$ = 0, and $\mathbf{F}^i(V_\infty, \alpha)$ is the *aerodynamic* force induced by the motion of the body. While $\mathbf{F}(V_\infty, \omega, \alpha)$ is the total resultant force acting on the body for free flight, $\mathbf{F}^w(\omega)$ is the tethered flight force that can be measured using conventional force/torque sensors, such as a load cell. Hence, $\mathbf{F}^i(V_\infty, \alpha)$ is the discrepancy between the real flight force and the tethered flight force. This is the main difference between fixed wing aerodynamic forces and flapping wing aerodynamic forces where fixed wing lift and drag forces are the functions of only the induced velocity and the angle of attack[2]. While both lift force and drag force become zero with V_∞ = 0 for fixed wing flight, the resultant force acting on a flapping wing body is still nonzero with V_∞ = 0. In this case, $\mathbf{F}^w(\omega)$ still produces the lift force for hovering while $\mathbf{F}^i(V_\infty, \alpha)$ = 0.

The equilibria of the system can be found with ($\dot{\phi}$, $\ddot{x}$, $\ddot{y}$) = (0, 0, 0) or ($\dot{\phi}$, $\ddot{x}_b$, $\ddot{y}_b$) = (0, 0, 0). From (1), (2), and (3), we can find only one equilibrium at F_N = 0, ϕ = 90°, and F_T = mg (or F_L = F_T = mg and F_D = F_N = 0). It is important to note that the system is pendulum-like passive stable at this equilibrium. Basically, for any small disturbance in the $\mathbf{e_n}$ direction, the body will start oscillating about the pitch axis and gradually approach ϕ = 0 with a slight fluctuation of $\dot{x}$ and $\dot{y}$. Therefore, F_N should be kept as small as possible to minimize pitch oscillation. An additional approach is to carefully choose the location of the center of mass so that the resultant force on the body directs toward $\mathbf{e}_t$ and the mean value of F_N vanishes. A stabilizer (or elevator) could be combined at the tail to actively damp out oscillations, but it requires more weight and more power.

[2]The lift force is $L = \frac{1}{2}C_L(\alpha)\rho u^2 S$ and the drag force is $D = \frac{1}{2}C_D(\alpha)\rho u^2$ S, where α is the angle of attack, u is the induced velocity, S is the reference area, and ρ is the air density which is constant for a small range altitude flight.

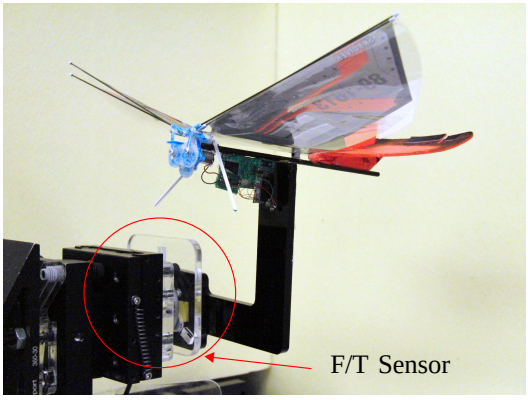

Fig. 4. Force measurement setup for an ornithopter with a load cell. The forces of the L bracket have been subtracted.

Assuming that the system stays near the stable equilibrium point, we are less interested in the identification of I and d since $\ddot{\phi} \simeq 0$. On the other hand, the identification of free flight aerodynamic forces is still important. With a closed-loop control where we can control the velocity of the ornithopter, i.e., both $\dot{y}$ and $\dot{x}$ are constants, we can easily estimate the force discrepancy, $\mathbf{F}^i$. For example, with $\ddot{y}$ = 0 and $\ddot{x}$ = 0 from (4) and (5), we have F_D = 0 and F_L = mg. Consequently, we have

$$F_L^i(V_\infty, \alpha) = mg - F_L^w(\omega) \quad (9)$$
$$F_D^i(V_\infty, \alpha) = -F_D^w(\omega) \quad (10)$$

Using the force measurement setup with a load cell (ATI Nano 43) as shown in Fig. 4, we have measured tethered flight forces, F_T^w and F_N^w. Fig. 5 shows an example of the measured forces with 80% PWM duty cycle. The fundamental frequency of the forces is indeed the flapping frequency of the wings. Although the peak to peak values are almost 0.6 N, the time average normal force and tangential force are only F_N^w = 18.15 mN and F_T^w = 94.95 mN, respectively. The total average force of 96.7 mN predicts the 12.4 gram ornithopter cannot lift itself at 80% duty cycle if V_∞ = 0.

Shown in Fig. 6 are the time average normal force, tangential force, and flapping speed of wings with various duty cycles. For these average values, we took steady state force measurement for 10 seconds with a 600 Hz sample rate. The circles in the plots are the measured data points and the solid lines are the first order polynomial fitted lines. The wing speed as well as forces are linear functions of the duty cycles in the range between 50% and 100% as shown in the plots.

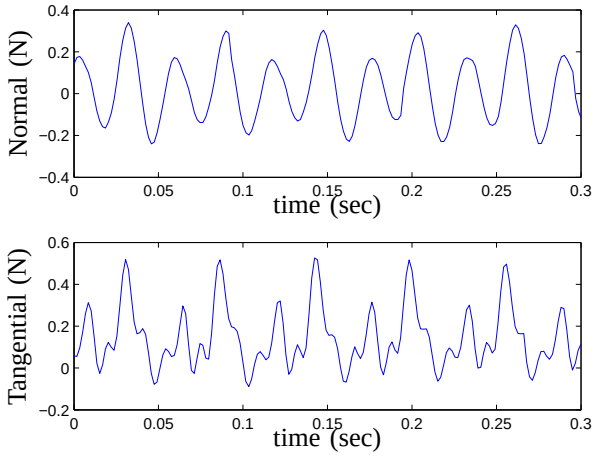

Fig. 5. Measurement of normal force (top) and tangential force (bottom) with 80% duty cycle. The average forces are 18.15 mN for normal and 94.95 mN for tangential.

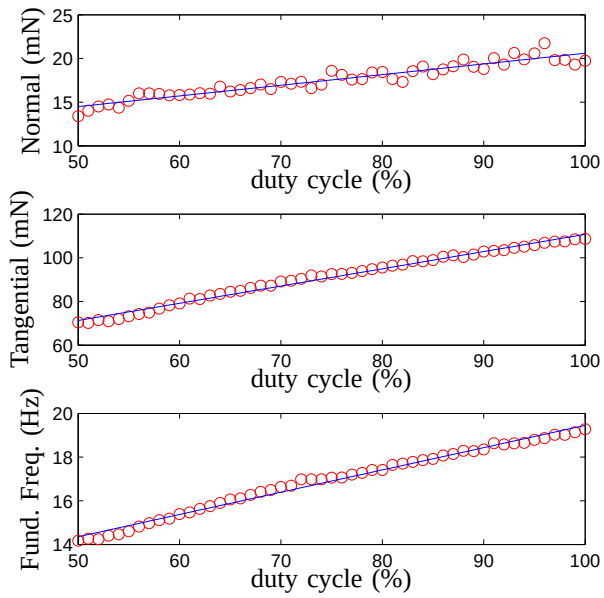

Fig. 6. The average normal force (top) , average tangential force (middle), and flapping speed of wings (bottom) with various duty cycles. The circles are the measured data points and the solid lines are first order polynomial fitted lines.

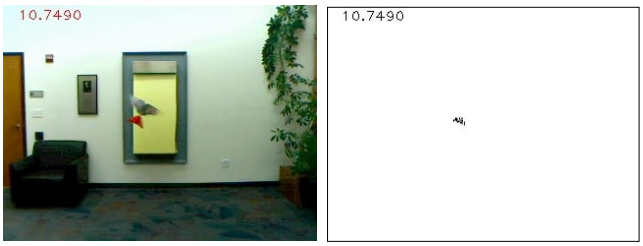

Fig. 7. A camera captured image of a free flying ornithopter (left) and the orange blob of the ornithopter found by the blob detection algorithm (right).

IV. TRACKING AND CONTROL METHODS

An external camera with the frame rate of 15 Hz and the resolution of 320×240 is connected to a PC to track the ornithopter. The resolution of 320×240 pixels with baseline of 3.8 meters gives pixel resolution of 1.2 cm at robot approximately. The tail of the ornithopter is painted in orange, and the Hue, Saturation, and Value (HSV) color model [12] is used to extract the orange blob from the image captured from the camera. The appropriate values of HSV depend on lighting conditions in an environment, and so they need to be chosen at the beginning of each experiment. Unlike the RGB color model, however, the Value component is the only variable in HSV that needs to be adjusted in most trials. To minimize the time spent for image processing, a Kalman filter has been implemented to predict the next blob position as follows

$$\mathbf{x}(k+1 \mid k) = \mathbf{x}(k) + T\mathbf{u}(k) + \mathbf{w}(k) \quad (11)$$

$$\mathbf{y}(k) = \mathbf{x}(k) + \mathbf{v}(k) \quad (12)$$

where $\mathbf{x}$ is the position vector, $\mathbf{u} = (\mathbf{x}(k) - \mathbf{x}(k-1))/T$ is the velocity vector, T = 67 ms is the time interval, $\mathbf{y}$ is the measured position vector, and $\mathbf{w}$ and $\mathbf{v}$ are independent white Gaussian noise. Here, $\mathbf{x}(k+1 \mid k)$ is the prediction of the next blob position. With this prediction, the blob detection algorithm based on OpenCV (Open Source Computer Vision) searches for an orange blob only in a small rectangular region (50×50 pixels or approximately 30×30 cm) centered at the predicted point by the Kalman filter. Fig. 7 shows the ornithopter image from the camera (left) and the blob detected by the algorithm (right) with $0 \leq$ Hue ≤ 13, $95 \leq$ Saturation ≤ 255, and $133 \leq$ Value ≤ 255.

Once the ground station estimates the center of the blob, the reference error between the estimated position and the desired position is computed. Then, the error value is sent to the ornithopter through a Bluetooth communication link with the baud rate of 230400 bps. The onboard microprocessor takes this data and computes the duty cycle of PWM signal using a PI controller shown in Algorithm 1. The proportional control gain K_p = 0.35 and the integral control gain K_i = 0.2 were determined by a trial and error method. The microprocessor, then, drives the motor board using the PWM signal to run the main flapping DC motor. The signal flow of this control law is summarized in Fig. 8.

V. EXPERIMENTAL RESULTS AND DISCUSSION

With an external camera as an altitude sensor, we have successfully achieved closed-loop height regulation of the ornithopter. Since steering control has not been implemented yet, the rudder is fixed in one direction so that the ornithopter always orbits around in the same direction in front of the camera. Fig. 9 shows a step response of the closed-loop system. The lateral motion (in the $\mathbf{E_1}$ direction) shows a pure sinusoidal curve with a slowly varying DC term, which

Algorithm 1 PI Controller for Duty Cycle (Γ)

previous error, $e^- \Leftarrow 0$
accumulated error, $\Sigma \Leftarrow 0$
maximum accumulated error, $\Sigma_{max} \Leftarrow 80$
minimum accumulated error, $\Sigma_{min} \Leftarrow$ -80
weight factor, $\lambda \Leftarrow 0.8$
duty cycle offset, $\Gamma_\circ \Leftarrow 82$
while True **do**
  receive error, e
  if $e = 0$ or sign(e) $\neq$ sign(e^-) **then**
    $\Sigma \Leftarrow 0$
  else
    $\Sigma \Leftarrow e + \lambda\Sigma$
  end if
  $\Sigma \Leftarrow$ min(max(Σ, Σ_{min}), Σ_{max})
  $\Gamma \Leftarrow K_p e + K_i \Sigma + \Gamma_\circ$
  $\Gamma \Leftarrow$ min(max(Γ, 0), 100)
  $e^- \Leftarrow e$
end while

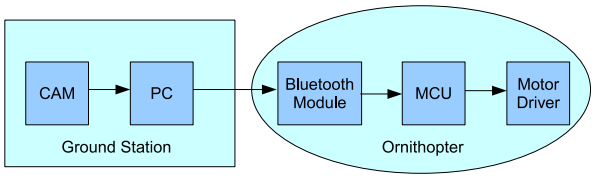

Fig. 8. Signal flow for closed-loop altitude regulation

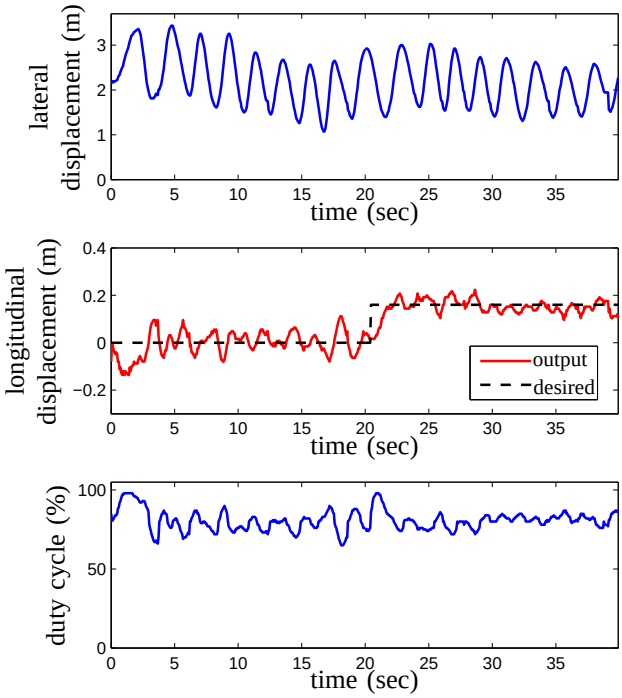

Fig. 9. Closed-loop step response of height regulation. (top) lateral displacement, (middle) longitudinal displacement and desired altitude, and (bottom) duty cycle for the driving DC motor.

indicates a lateral drift due to external disturbances, such as an indoor breeze. The sinusoidal curve with a nearly constant frequency and constant peak-to-peak amplitude indicates a constant speed in lateral direction. The longitudinal displacement and the desired altitude are also shown. The maximum error in the plot is only about 10 cm, which is located at $t \approx 18$ sec. The error after t = 20 sec. is less than 3 cm. The average duty cycle for the DC motor is 80% for this experiment. A sequence of video frames in the range between t = 32.51 sec and t = 33.53 sec is shown in Fig. 10. The solid cyan circles are the locations of orange tails detected by the blob tracking algorithm and the white horizontal lines in the middle of frames indicate the desired altitude.

The orbital motion of the ornithopter was the result of the force on the rudder fixed in one direction, not the result of wing motions or induced velocity. With a nearly constant lateral speed, therefore, it is still safe to assume that $\ddot{x}$ due to F_L and F_D is close to zero [3]. Also the average longitudinal acceleration in the range between t = 25 sec and t = 33

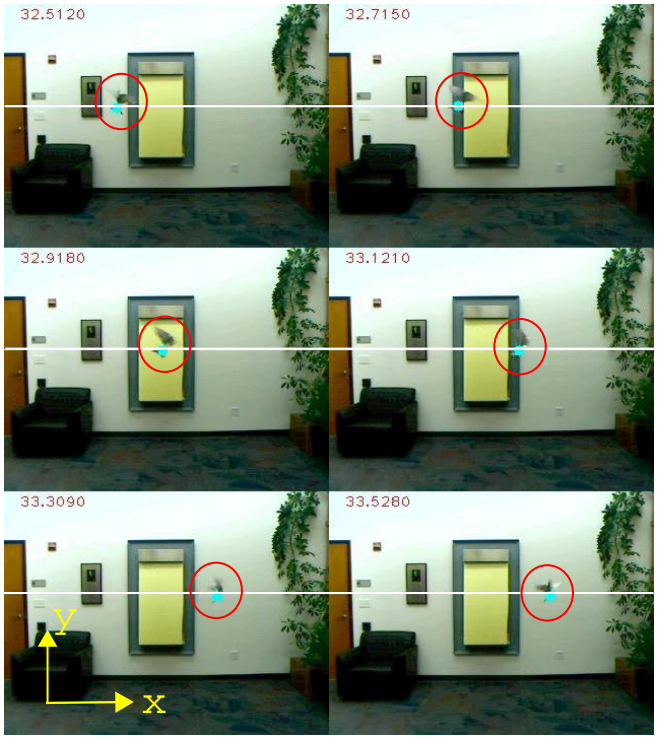

Fig. 10. A sequence of video frames shows successful altitude control. The solid cyan circles are the locations of orange tails detected by the blob tracking algorithm. The white horizontal lines in the middle of frames indicate the desired altitude.

[3]The centripetal acceleration V^2/r, where V is the constant lateral speed and r is the constant orbital radius, is provided solely by the force on the rudder. The other component of the acceleration in the tangential direction is $\dot{V} = 0$.

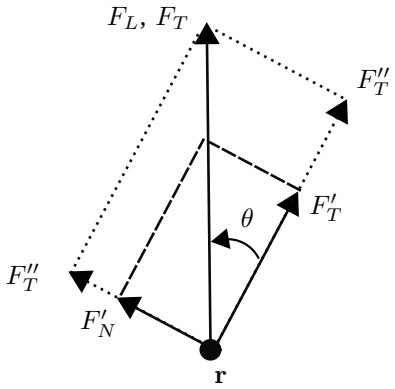

Fig. 11. Diagram of actual forces and measured forces

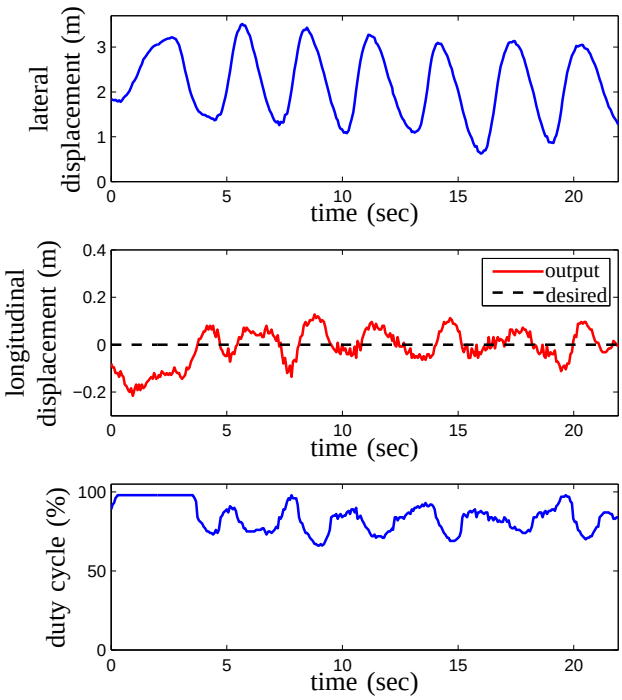

Fig. 12. Closed-loop step response of height regulation with an added mass. (top) lateral displacement, (middle) longitudinal displacement and desired altitude, and (bottom) duty cycle for the driving DC motor.

sec is close to zero [4]. From this result and the inspection of images taken by the camera, we know that $\dot{\phi} = 0$ and the free flight aerodynamics forces are $F_D = 0$ and $F_L = mg = 121.5$ mN. As discussed in Section III, at this equilibrium point, we have $\phi = 90°$, $F_L = F_T = mg$, and $F_D = F_N = 0$. From the load cell measurement, however, we have $F_N^w = 18.15$ mN and $F_T^w = 94.95$ mN. The difference here indicates that (1) the force vectors for measurement did not agree with the actual tangential and normal force vectors (2) the tethered measurement underestimated the flight forces. Fig. 11 shows the actual force vectors and the measured force vectors (F'_T, F'_N). In order to fix the measurement, we must first find the angle θ between the actual flight forces and measured flight forces. We have $\theta = \tan^{-1}(F'_N/F'_T) = 10.8°$ in this case. The magnitude of the sum of two vectors (F'_N, F'_T) is 96.7 mN. From this result, we know that tethered measurement with zero induced velocity underestimates the lift force by F_L^i = 121.5 - 96.7 = 24.8 mN at 80% duty cycle. F''_T -F'_T and F''_N-F'_N are the underestimated forces in the measurement coordinates.

Shown in Fig. 12 are the response of height regulation with an added mass of 0.34 grams. It shows an oscillatory longitudinal response due to the changes in pitch angle. Because of the added mass, the system needs to generate a larger lift force, which is coupled with the drag force. This larger drag force results in larger oscillatory behavior of pitch angle.

VI. CONCLUSIONS AND FUTURE WORK

In this paper, we have discussed implementation of closed-loop altitude control of a flapping wing micro air-vehicle using an external camera for altitude measurement. We also demonstrated an analysis of flight forces acting on flapping wing robots to explain the deviation between the measured forces and the free flight forces. Using this analysis and the height regulation, we have identified that tethered aerodynamic force measurement of a 12.4 gram ornithopter with zero induced velocity underestimates the total force by 24.8 mN, likely due to the absence of induced velocity and the tether restraining the body.

We are currently developing a 1.0 gram microprocessor board consisting of a 3-axis accelerometer, a 3-axis gyroscope, a 2-channel motor driver, and a 2.4 GHz wireless transceiver. This new microprocessor board will enable us to directly measure free flight aerodynamic forces and estimate the orientation of the ornithopter. It will also reduce the total weight of the ornithopter from 12.4 grams to 11.4 grams, which will provide an extra 1.0 gram payload. Cooperating with a motion tracking system using external high speed cameras or a Vicon motion capturing system, we believe we can identify system parameters of ornithopters more accurately.

VII. ACKNOWLEDGMENTS

The authors would like to thank Fernando Garcia Bermudez for his help with the microprocessor board and the Bluetooth module, Paul Birkmeyer and Kevin Ma for their help with editing pictures, and Aaron Hoover for his Python codes for reliable Bluetooth communication. This material is based upon work supported by the National Science Foundation under Grant No. IIS-0705429. Any opinions, findings and conclusions or recommendations expressed in this material are those of the authors and do not necessarily reflect the views of the National Science Foundation (NSF).

[4]Due to the vibratory nature of flapping mechanisms, there are always nonzero body accelerations at a high frequency, but the accelerations at a low frequency ($<$ 1 Hz) at hovering could be zero.

REFERENCES

[1] S. Avadhanula, R. Wood, E. Steltz, J. Yan, and R. Fearing, "Lift force improvements for the micromechanical flying insect," in *IEEE/RSJ Int. Conf. on Intelligent Robots and Systems*, October 2003.

[2] X. Deng, L. Schenato, and S. S. Sastry, "Flapping flight for biomimetic robotic insects: part ii-flight control design," vol. 22, no. 4, pp. 789–803, 2006.

[3] R. Fearing, K. Chiang, M. Dickinson, D. Pick, M. Sitti, and J. Yan, "Wing transmission for a micromechanical flying insect," in *IEEE Int. Conf. on Robotics and Automation (ICRA)*, April 2000.

[4] F. Garcia Bermudez and R. Fearing, "Optical flow on a flapping wing robot," in *IROS'09: Proceedings of the 2009 IEEE/RSJ international conference on Intelligent robots and systems*. IEEE Press, 2009, pp. 5027–5032.

[5] Y. Kawamura, S. Souda, S. Nishimotor, and C. Ellington, *Biomechanisms of Swimming and Flying: Fluid Dynamics, Biomimetic Robot, and Sports Science*. Springer, 2008, ch. 26: Clapping-wing Micro Air Vehicle of Insect Size, pp. 319–330.

[6] Z. A. Khan and S. K. Agrawal, "Design and optimization of a biologically inspired flapping mechanism for flapping wing micro air vehicles," in *IEEE International Conference on Robotics and Automation*, Rome, Italy, April 2007.

[7] D. Lentink, "Exploring the biofluiddynamics of swimming and flight," Ph.D. dissertation, Wageningen University, 2008.

[8] D. Lentink, S. R. Jongerius, and N. L. Bradshaw, *Flying Insects and Robots*. Springer, 2009, ch. 14: The Scalable Design of Flapping Micro-Air Vehicles Inspired by Insect Flight, pp. 185–205.

[9] Q.-V. Nguyen, H. Park, N. Goo, and D. Byun, "A flying insect-like flapper actuated by a compressed LIPCA," in *IEEE International Conference on Robotics and Biomimetics*, December 2007, pp. 19 – 24.

[10] J. H. Park and K.-J. Yoon, "Designing a biomimetic ornithopter capable of sustained and controlled flight," *Journal of Bionic Engineering*, vol. 5, no. 1, pp. 39–47, March 2008.

[11] K. S. Shigeoka, "Velocity and altitude control of an ornithopter micro aerial vehicle," Master's thesis, The University of Utah, 2007.

[12] A. R. Smith, "Color gamut transform pairs," in *SIGGRAPH 78*, August 1978.

[13] F. van Breugel, Z. E. Teoh, and H. Lipson, *Flying Insects and Robots*. Springer, 2009, ch. 13: A Passively Stable Hovering Flapping Micro-Air Vehicle, pp. 171–184.

[14] R. J. Wood, "Liftoff of a 60mg flapping-wing MAV," in *IEEE/RSJ International Conference on Intelligent Robots and Systems*, San Diego, CA, 2007.

[15] R. J. Wood and R. S. Fearing, "Flight force measurements for a micromechanical flying insect," in *IEEE/RSJ International Conference on Intelligent Robots and Systems*, Maui, HI, November 2001.